LOG-LIO: A LiDAR-Inertial Odometry with Efficient Local Geometric Information Estimation

Kai Huang¹, Junqiao Zhao*,2,3, Zhongyang Zhu^{2,3}, Chen Ye², Tiantian Feng¹

Abstract—Local geometric information, i.e. normal and distribution of points, is crucial for LiDAR-based simultaneous localization and mapping (SLAM) because it provides constraints for data association, which further determines the direction of optimization and ultimately affects the accuracy of localization. However, estimating normal and distribution of points are time-consuming tasks even with the assistance of kdtree or volumetric maps. To achieve fast normal estimation, we look into the structure of LiDAR scan and propose a ringbased fast approximate least squares (Ring FALS) method. With the Ring structural information, estimating the normal requires only the range information of the points when a new scan arrives. To efficiently estimate the distribution of points, we extend the ikd-tree to manage the map in voxels and update the distribution of points in each voxel incrementally while maintaining its consistency with the normal estimation. We further fix the distribution after its convergence to balance the time consumption and the correctness of representation. Based on the extracted and maintained local geometric information, we devise a robust and accurate hierarchical data association scheme where point-to-surfel association is prioritized over point-to-plane. Extensive experiments on diverse public datasets demonstrate the advantages of our system compared to other state-of-the-art methods. Our open source implementation is available at https://github.com/tiev-tongji/LOG-LIO.

I. INTRODUCTION

Simultaneous localization and mapping (SLAM) plays an important role in autonomous driving and robotics tasks. Compared with visual-inertial systems [1]–[3], LiDAR (-inertial) systems [4]–[6] are more robust and accurate because they are less sensitive to illumination changes, can obtain accurate depth, and have a larger field of view (FoV).

The performance of LiDAR-based system depends heavily on the registration between the LiDAR scan and the map, i.e. finding the correspondence between them based on the similarity of the local geometric information and then minimizing their distance. Local geometric information includes attributes that can represent the position, shape, and other characteristics of the local surface where a point is located.

 1 Kai Huang and Tiantian Feng are with the School of Surveying and Geo-Informatics, Tongji University, Shanghai, China (e-mail: huangkai@tongji.edu.cn; fengtiantian@tongji.edu.cn).

²Junqiao Zhao, Zhongyang Zhu and Chen Ye are with Department of Computer Science and Technology, School of Electronics and Information Engineering, Tongji University, Shanghai, China, and the MOE Key Lab of Embedded System and Service Computing, Tongji University, Shanghai, China (e-mail: zhaojunqiao@tongji.edu.cn; 1930773@tongji.edu.cn; yechen@tongji.edu.cn).

³Institute of Intelligent Vehicles, Tongji University, Shanghai, China This work is supported by the National Key Research and Development Program of China (No. 2021YFB2501104). (*Corresponding Author: Junquao Zhao.*)

In LiDAR-based systems, the conventional method for estimating local geometric information is to evaluate the smoothness of the input scan and to locally approximate the map with geometric primitives [7]. However, accurate estimation of local geometric information requires the retrieval of neighborhood information in a dense point cloud, but for LIO systems this results in a huge computational burden even with the help of kdtree or volumetric maps.

Accurate and fast estimation of local geometric information has gained increasing attention in recent studies [5], [6], [8]–[10]. Among them, the normal and the distribution of points are two representative attributes, since the former indicates the tangent plane of the local surface, and the latter implies the average position and shape of the point cloud sampled from the local surface. However, current LIO systems seldom incorporate the help of real-time estimation of the normal and the distribution of points, which hampers their pose estimation performance.

This paper presents LOG-LIO, a robust and accurate LIO system focusing on the real-time estimation of the normal of LiDAR scan points and the distribution of map points, and their rational utilization. Inspired by [11] and [12], we look into the structure of a LiDAR scan and propose a Ring-based fast approximate least squares method, namely Ring FALS. We project point cloud onto the range image to pre-build a lookup table, which represents the structural information of the specific LiDAR. With the arrival of a new scan, only the range information of the points is needed to estimate the normal. We incrementally update the distribution of points for each voxel in the map while maintaining its consistency with the normals. To balance time consumption and correctness of representation, we manage the map on the extended ikd-tree and further fix the distribution after it converges.

Similar to the FAST-LIO series [13], [14], we directly associate scan points with voxels on the map after distortion correction. For scan points that satisfy visibility and consistency checks based on normals, we devise a robust and accurate hierarchical data association scheme considering the distribution. The poses are optimized by integrating the IMU measurements as initial estimates and then using an error-state iterative Extended Kalman filter (iEKF) [13] to minimize the multi-scale point-to-surfel and point-to-plane distances.

The main contributions of this work are as follows:

 Ring FALS, modified from FALS, a normal estimator that utilizes the structural information of LiDAR scan can meet the real-time requirements of the LIO system.

- A robust and accurate hierarchical data association scheme considering the distribution of points within map voxels where point-to-surfel is prioritized over point-to-plane and large-scale surfel over small-scale surfel.
- Extensive experiments on public datasets demonstrate
 the advantages of our LIO system compared to other
 state-of-the-art methods. To benefit the community,
 our implementation of this work is open-source at
 https://github.com/tiev-tongji/LOG-LIO, and we also
 open-source Ring FALS as an independent normal tool
 at https://github.com/tiev-tongji/RingFalsNormal.

II. RELATED WORKS

A. Point Cloud Normal Estimation

The most commonly used method to obtain surface normals from point cloud is the least square estimation based on the neighborhood search due to its ease of implementation [15]. However, the least squares-based method is computationally expensive for LIO systems.

[11] compares the complexity of least squares approaches and proposes fast approximate least squares (FALS), which simplifies the least squares loss function to completely avoid the computation of the covariance matrix for each point. [11] also reformulates the traditional least squares solution to estimate the normal by calculating the derivatives of the surface from a spherical range image (SRI). However, the number of multiplications for normals computation of SRI is greater than FALS.

Rather than least square-based solution, 3F2N [12] performs three filtering operations on the inverse depth image to estimate the normals, which has the comparative performance as FALS, but its efficiency and accuracy are strongly influenced by the filter selection.

Inspired by [11] and [12], we propose Ring FALS. We pre-build a lookup table which represent the structural information for the specific LiDAR. Compared to FALS, Ring FALS further simplifies the projection of each LiDAR scan with the assistance of ring index, while preserving accuracy.

B. Distribution of Points Estimation

The distribution of a point is represented through its 3D coordinates and the covariance matrix computed by its neighboring points. [16] proposes the generalized ICP (GICP) algorithm, which takes into account the locally planar structure of points in a probabilistic model and then minimizes the distance between distributions. But searching neighboring points to compute the covariance matrix is too time-consuming for LIO systems.

LOAM [7] does not estimate the distribution of points, but performs Eigen analysis on the associated map points to determine whether its local geometry is a line or a plane. However, the coordinates of the sparse map points cannot accurately represent the local geometric information, which leads to inaccurate constraints for the registration.

DLO [5] registers point cloud using GICP to minimize the plane-to-plane distance, which is derived from the covariance

matrix of each point. It assumes that the covariance of submap can be approximated by concatenating the normals from keyframes, and the covariance of points is only computed once when the scan is acquired. However, such a normals stitching method cannot accurately reflect the local geometric information of the point cloud, which ultimately affects accuracy. LOCUS 2.0 [8] extends the work of LOCUS [9], which constructs covariance matrices for GICP-based registration based on the pre-computed normals, but how to pre-compute normals is not elaborated in their paper.

Wildcat [10] fits ellipsoids based on the coordinates and timestamps of the clustered points. The ellipsoids representing the distribution of points are further used to generate surfels. SLICT [6] further proposes an octree-based global map and updates the distribution of points within each voxel incrementally. It obtains large-scale distributions by merging multiple voxels to generate surfels in multi-resolution.

Inspired by the above methods, we extend ikd-tree to maintain the distribution of points in each map node incrementally, and fix the distribution after its convergences.

C. LiDAR (-Inertial) Odometry

LOAM [7] has inspired many LiDAR SLAM systems due to the low coupling of system modules and the rational use of point cloud geometry attributes. However, the lack of effective map management and the high time consumption required for optimization can degrade the performance of the system.

LIO-SAM [17] proposes a framework based on keyframes and local maps, which optimizes poses in a factor graph. However, LIO-SAM builds sub-maps for input scans by simply merging point cloud of surrounding keyframes, which is a time-consuming process when the number of points is large compared to incrementally maintaining maps.

FAST-LIO [13] employs point-to-plane correspondence and the iEKF to directly register the LiDAR scan and the map. It presents a new formula to compute the Kalman gain, and the computation load only depends on the dimension of state dimension. FAST-LIO2 [14] maintains the map by an incremental kdtree data structure, namely ikd-tree, to further improve efficiency.

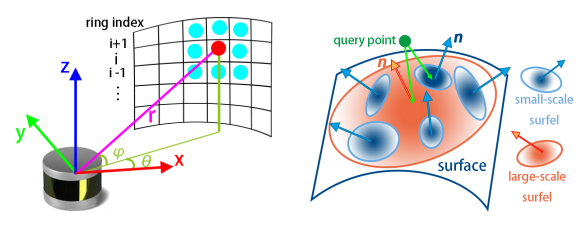
In this paper, we also adopt the iEKF to optimize poses by directly registering the LiDAR scan and the map, but with a different data association scheme. By incorporating real-time normal and distribution of points estimation, we can efficiently construct surfels in multi-scale, which represent the geometry of local surface more accurately than other geometric primitives, e.g. plane. We prioritize associating large-scale surfels over small-scale surfels since large-scale surfels are modeled using more points and are insensitive to noise.

III. PRELIMINARY

A. Notation

We now define notations and frames that we used throughout the paper. We consider W as the world frame and \mathcal{I}_k , \mathcal{L}_k as the IMU and LiDAR frames, related to the k-th LiDAR scan at time t_k , respectively. ${}^a\mathbf{T}_b \in SE(3)$ to be Euclidean transformation take 3D points from frame b to frame a, which is consisted of rotation ${}^a\mathbf{R}_b \in SO(3)$ and translation ${}^a\mathbf{t}_b \in \mathbb{R}^3$. n_r denotes the normal from Ring FALS and e_d is the eigenvector corresponding to the smallest eigenvalue of a distribution (see Section III-D).

B. LiDAR Observation Model



(a) LiDAR observation model (b) multi-scale surfel association

Fig. 1. Illustration of the LiDAR observation model and multi-scale surfel association. (a) The magenta line indicates the ray of the red point. The eight points are the neighborhoods that Ring FALS uses to estimate the normal of the red point. (b) The five blue ellipses represent the small-scale surfels of the nearest voxels corresponding to the green query point in the extended ikd-tree. The orange ellipses represent the large-scale surfel merged by the small-scale surfels. The green query point is first associated with the large-scale surfel. If the large-scale surfel cannot meet the criteria in Section III-D and Section V-B.3, it is then associated with the small-scale surfel of the voxel where it is located.

In practice, LiDAR obtains the 3D coordinates of a point by combining bearing and range measurements of the target surface [18], [19], as shown in Figure 1(a). The LiDAR observation model is as follows:

$$\mathbf{p}_{i} = r_{i}\mathbf{v}_{i} = r_{i} \begin{bmatrix} \cos\theta_{i}\cos\varphi_{i} \\ \sin\theta_{i}\cos\varphi_{i} \\ \sin\varphi_{i} \end{bmatrix}$$
(1)

where r_i is the range, θ_i the azimuth and φ_i the vertical angle of the target point. v represents the horizontal and vertical structural information of the point relative to the LiDAR.

For a spinning LiDAR, the scan points can also be arranged into a mapping table \mathcal{T} based on their ring index and azimuth relative to the LiDAR as follows:

$$\mathbf{p}_i = \mathcal{T}(row_i, column_j, r_i)$$
 (2)

where $row_i = ring(\mathbf{p}_i)$ and $column_j = \theta_i$.

C. Least Squares Normal Estimation

Given a subset of n 3D points p_i , i=1,2,...,n of the surface, least squares finds the normal vector $\boldsymbol{n}=(n_x,n_y,n_z)$ and the scalar d that minimizes Equation (3).

$$e = \sum_{i=1}^{n} (\boldsymbol{p}_{i}^{T} \boldsymbol{n} - d)^{2}$$
(3)

The closed form solution of the normal n is the eigenvector corresponding to the smallest eigenvalue of the covariance matrix in Equation (4).

$$M = \sum_{i=1}^{n} (\mathbf{p}_i - \overline{\mathbf{p}})(\mathbf{p}_i - \overline{\mathbf{p}})^T$$
 (4)

with $\overline{p} = 1/n \sum_{i=1}^{n} p_i$.

D. Surfel

We define the planarity ρ within a voxel similar to SLICT [6], and further introduce γ as following:

$$\rho_i = 2(\lambda_2 - \lambda_1)/(\lambda_1 + \lambda_2 + \lambda_3)$$

$$\gamma_i = \lambda_2/\lambda_1$$
(5)

where $\lambda_1, \lambda_2, \lambda_3$ are the eigenvalues of covariance matrix M with $\lambda_1 < \lambda_2 < \lambda_3$. We define a voxel representing a surfel has ρ_i greater than 1.0 and γ_i greater than 100, where a larger ρ_i implies that the distribution of the sampled points is flatter on the surface, and a larger γ_i indicates that the distribution is less close to a linear geometry. A surfel is represented by the mean position of points \overline{p} within the voxel and the normal e_d , where e_d is the eigenvector corresponding to λ_1 . Multiple small-scale surfels can be merged into a large-scale surfel by merging the distribution as shown in Figure 1(b) (detailed in Section IV-B).

IV. LOCAL GEOMETRIC INFORMATION EXTRACTION

In this section, the efficient extraction of two representative attributes of local geometric information, i.e. normal and distribution of points are introduced.

A. Ring FALS Normal Estimator

We first revisit FALS [11]. In FALS, Equation (3) is reformulated to obtain:

$$\widetilde{e} = \sum_{i=1}^{n} (\boldsymbol{p}_i^T \widetilde{\boldsymbol{n}} - 1)^2$$
 (6)

where \tilde{n} is defined up to a scale factor. Substituting Equation (1) gives:

$$\widetilde{e} = \sum_{i=1}^{n} r_i^2 (v_i^T \widetilde{n} - r_i^{-1})^2$$
 (7)

where r_i is the range and v_i implies the bearing information of the target points related to the LiDAR.

It can be assumed that the range of points within a small region are similar, thanks to the high-resolution LiDAR. Therefore, r_i^2 can be removed from Equation (7) to obtain an approximation:

$$\hat{e} = \sum_{i=1}^{n} (\mathbf{v}_{i}^{T} \hat{\mathbf{n}} - r_{i}^{-1})^{2}$$
(8)

where $\widehat{\boldsymbol{n}}$ is the approximate normal, and it has the closed form solution $\widehat{\boldsymbol{n}} = \widehat{\boldsymbol{M}}^{-1}\widehat{\boldsymbol{b}}$ where $\widehat{\boldsymbol{M}} = \sum_{i=1}^n v_i v_i^T$ and $\widehat{\boldsymbol{b}} = \sum_{i=1}^n v_i/r_i$. The matrix $\widehat{\boldsymbol{M}}^{-1}$ depends only on the constant structural information \boldsymbol{v} , independent of the range \boldsymbol{r} . Hence, the matrix $\widehat{\boldsymbol{M}}^{-1}$ can be pre-computed as a lookup table.

To obtain the neighborhood of v_i for computing \widehat{M}^{-1} and \widehat{b} , FALS projects the LiDAR scan points onto an SRI following Equation (1). The computation of \widehat{M}^{-1} and \widehat{b} requires that each pixel in the SRI has a corresponding measurement, hence an interpolation is needed since the LiDAR scan points only occupy sparse pixels. This is in turn a time-consuming process.

Different from FALS, Ring FALS establishes a fast mapping following Equation (2) based on the structural information of the LiDAR. To avoid the expensive vacant pixel interpolation, we create a table with the number of rows and columns equal to the number of rings and the number of points within each ring, respectively. As a result, Ring FALS speeds up the projection procedure in FALS.

By pre-computing the lookup table, normal estimation avoids the slow neighborhood searching process in many LIO systems. And a dense normal estimation for LiDAR scan can be achieved. Moreover, we flip all the backfaced normals and then apply image blurring to smooth the normals and improve their consistency.

B. Distribution of Points Estimation

Most LIO systems rely on point cloud maps, but the sparsity of map points results in inaccurate constraints and degrades the accuracy of pose estimation. Rather than using the point cloud map, we adopted an incremental approach to maintaining the distribution of points within each voxel like SLICT [6].

The distribution of points within a voxel can be represented by its mean position \overline{p} and the covariance matrix M, as shown in Equation (4). And M can be further simplified as follows:

$$M = \mathcal{S}_n - \frac{1}{n} \mathcal{P}_n \mathcal{P}_n^T \tag{9}$$

where S_n denotes $\sum_{i=1}^n p_i p_i^T$ and P_n denotes $\sum_{i=1}^n p_i$. Due to the symmetric nature of M, it is only necessary to record the six elements in its upper right corner.

The accurate representation of the distribution of points requires a large number of points. Due to limited resolution and occlusion, point cloud from multiple locations must be accumulated incrementally to obtain high quality maps. For newly incorporated m points in a voxel, their \mathcal{S}_m , \mathcal{P}_m need to be calculated. Subsequently, the distribution of points within this voxel can be updated by:

$$\overline{\boldsymbol{p}} = (\mathcal{P}_n + \mathcal{P}_m)/(n+m)$$

$$\boldsymbol{M} = \mathcal{S}_n + \mathcal{S}_m - \frac{1}{n+m}(\mathcal{P}_n + \mathcal{P}_m)(\mathcal{P}_n + \mathcal{P}_m)^T$$
 (10)

Equation (10) is also employed to generate distributions in multi-scale.

To balance computational efficiency and accuracy, we limit the number of points added to each voxel by tuning the downsampling rate in pre-processing. Additionally, we consider the distribution stabilizes once the directions of n_r (introduced in V-A) and e_d converge. The distribution is then fixed in the map.

V. SYSTEM DESCRIPTION

The pipeline of LOG-LIO is shown in Figure 2. For a new input scan, we first estimate the normal of the points. The association is then performed between the undistorted point cloud and the map according to their local geometric information. We incorporate the measurements of IMU and optimize the poses of the body via iEKF. After optimization, new points are added to the map managed by the extended

ikd-tree, and the distribution within a voxel is incrementally maintained.

Our system takes the IMU frame as the body frame, where the system state x can be written as:

$$\mathbf{x} = \begin{bmatrix} {}^{\mathcal{W}}\mathbf{R}_{\mathcal{I}}^T \ {}^{\mathcal{W}}\mathbf{p}_{\mathcal{I}}^T \ {}^{\mathcal{W}}\mathbf{v}_{\mathcal{I}}^T \ \mathbf{b}_{\omega}^T \ \mathbf{b}_{a}^T \ {}^{\mathcal{W}}\mathbf{g}^T \end{bmatrix}$$
(11)

where ${}^{\mathcal{W}}\mathbf{R}_{\mathcal{I}}^{T}$, ${}^{\mathcal{W}}\mathbf{p}_{\mathcal{I}}^{T}$ and ${}^{\mathcal{W}}\mathbf{v}_{\mathcal{I}}^{T}$ are the orientation, position and velocity of IMU in the world frame (i.e. the first IMU frame), \mathbf{b}_{ω}^{T} and \mathbf{b}_{a}^{T} are gyroscope and accelerometer bias respectively, ${}^{\mathcal{W}}\mathbf{g}^{T}$ is the known gravity vector in the world frame

A. Data Pre-processing

LOG-LIO uses Ring FALS (Section IV-A) to to estimate the normal for each input point, denoted as n_r . Subsequently, voxel grid downsampling and backward propagation based on IMU measurements are used for point reduction and distortion correction, respectively.

B. Data Association

At the beginning of data association, the IMU measurements are integrated from the previous frame to predict the pose $\hat{\mathbf{x}}_k$. Using this prediction, each new input point $^{\mathcal{L}}\boldsymbol{p}_i$ is transformed to the world frame $^{\mathcal{W}}\boldsymbol{p}_i = ^{\mathcal{W}} \hat{\boldsymbol{T}}_{\mathcal{I}} ^{\mathcal{I}} \boldsymbol{T}_{\mathcal{L}} ^{\mathcal{L}} \boldsymbol{p}_i$. Then, data association is performed in three consecutive steps:

- 1) Initial Correspondence: For a query point ${}^{\mathcal{W}}\mathbf{p}_i$, we first search for its k nearest map points corresponding to k nearest map voxels.
- 2) Visibility and Consistency Checks: The candidate associated map points may not be visible to the LiDAR if the angle between the normal of the map point and the ray (vector from the query scan point to the LiDAR center) is greater than 90 degrees. Such a case usually occurs indoors, where the two planes of an object (e.g. a wall) are close to each other, which is referred to as the double-side issue [20]. This incorrect correspondence is eliminated directly.

The consistency of the associated map points is evaluated by computing the average angle between the normal of the query point and the normals of the associated map points. If the average angle is larger than a threshold α ($\alpha=60^\circ$ in this paper), we consider it an inconsistent association and discard it.

3) Hierarchical Association: For query points satisfying visibility and consistency checks, a hierarchical association is performed, where point-to-surfel is prioritized over point-to-plane, and large-scale surfels are prioritized over small-scale surfels.

Surfel is a more precise and flexible representation of a local surface than a plane fitted with sparse map points because surfel is modeled with the distribution of points, which implies not only the location but also the shape of the local surface. Large-scale surfel can be approximated by merging multiple small-scale distributions (Figure 1(b)) and is insensitive to noise, thus providing more robust constraints than small-scale surfel. However, if the associated map points do not lie in the large-scale surfel (i.e. distance between any map point to the surfel is large than a threshold), we consider

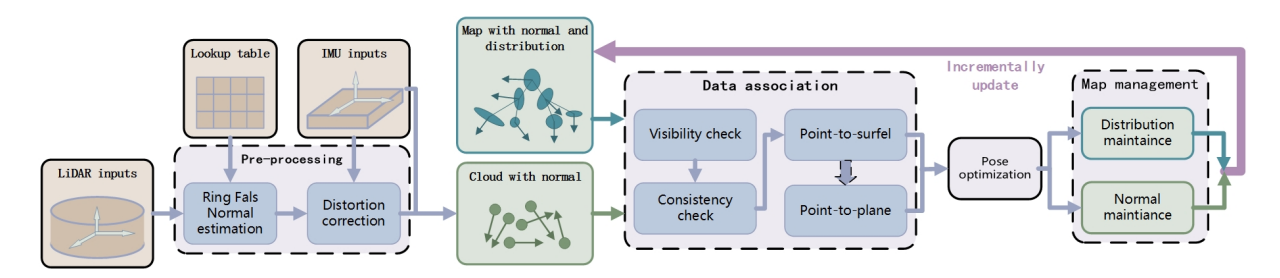


Fig. 2. System overview of LOG-LIO

the large-scale surfel to be of low quality. Instead, association with small-scale surfels is adopted.

For constraints with small-scale surfels, we associate the query point with the surfel of the voxel where the point is located, which must already be fixed. If the voxel cannot meet the criteria of a surfel (Section III-D), we resort to using the point-to-plane association.

C. Pose optimization

We adopt the iEKF from FAST-LIO2 to optimize the pose. The prediction step is implemented by the integration of IMU measurements from the latest optimized state $\overline{\mathbf{x}}_{k-1}$ along with the covariance matrix $\overline{\mathbf{P}}_{k-1}$.

For the residual computation, given a point ${}^{\mathcal{W}}\mathbf{p}_i$ in the world frame, the residual z_i is calculated as:

$$\mathbf{z}_i = \boldsymbol{n}_j(^{\mathcal{W}}\boldsymbol{p}_i - ^{\mathcal{W}}\boldsymbol{q}_j) \tag{12}$$

where n_j is the normalized normal of the associated surfel or plane for p_i , and $^{\mathcal{W}}q_j$ is a point lying on the associated element.

Then, we denote the propagated state and covariance by $\widehat{\mathbf{x}}_k$ and $\widehat{\mathbf{P}}_k$ respectively. They represent the prior Gaussian distribution for the state. By incorporating the prior distribution and the measurement models for point-to-surfel and point-to-plane associations from Equation (12), we obtain the maximum a-posterior estimate (MAP) as follows:

$$\min_{\widetilde{\mathbf{x}}_{k}^{\kappa}} (\|\mathbf{x}_{k} \boxminus \widehat{\mathbf{x}}_{k}\|_{\widehat{\mathbf{P}}_{k}}^{2} + \sum_{i \in surfel} \|\mathbf{z}_{i}^{\kappa} + \mathbf{H}_{i}^{\kappa} \widetilde{\mathbf{x}}_{k}^{\kappa}\|_{\mathbf{R}_{i}}^{2} + \sum_{j \in plane} \|\mathbf{z}_{j}^{\kappa} + \mathbf{H}_{j}^{\kappa} \widetilde{\mathbf{x}}_{k}^{\kappa}\|_{\mathbf{Q}_{j}}^{2})$$
(13)

where $\widetilde{\mathbf{x}}_{k}^{\kappa}$ is the error of the κ -th iterate update at time k, \mathbf{H}_{i}^{κ} and \mathbf{H}_{j}^{κ} are Jacobian matrices with respect to $\widetilde{\mathbf{x}}_{k}^{\kappa}$, \mathbf{R}_{i} and \mathbf{Q}_{j} come from the raw measurement noise. The Kalman gain can be computed efficiently, with the computation load depending on the state dimension instead of the measurement dimension [13], [14].

D. Map Management

LOG-LIO manages maps with an extended ikd-tree and voxels, and assigns each voxel to a corresponding tree node. To address the computational burden caused by recalculating the distribution of points when new points are added to a voxel, we incrementally maintain the distribution of points within each voxel as described in Section IV-B.

VI. EXPERIMENTAL RESULTS

A. Implementation details

For each node of the extended ikd-tree, we maintain the distribution of points after the number of points in the voxel has accumulated to $\eta=25$. The downsampling grid in data pre-processing is set to have the same size as the map to ensure that at most one point falls within a voxel for each frame. As long as the angle between n_r and e_d is less than 20 degrees, the distribution is considered to be stabilized, then the n_r and e_d are both fixed as the average of them. For a map voxel that accumulated 2η points but remains unfixed, we consider that its distribution no longer needs to be updated and fix it.

B. Experimental Settings

The experiment focuses on the following two research questions:

- Can Ring FALS estimates the normal of LiDAR points in real-time and accurately represents environmental information?
- Can LOG-LIO improve the accuracy of pose estimation by incorporating normal and distribution of points estimation?

We conduct extensive experiments on the public datasets M2DGR [21] and NTU VIRAL [22] to answer the above two questions. Both datasets have 9-axis IMU measurements and ground truth trajectories. The M2DGR dataset collects data on a ground platform equipped with Velodyne-32 LiDAR and captured in diverse scenarios including both indoor and outdoor environments. The ground truth trajectories are obtained by a laser 3D tracker, a motion capture device and an RTK receiver. The NTU VIRAL dataset collects data on an Unmanned Aerial Vehicle (UAV) platform with ground truth obtained by a laser-tracker total station with centimeter-level accuracy. The horizontal Ouster 16-channel OS1 LiDAR and VectorNav VN100 IMU are used. Compared with M2DGR, the LiDAR used by VIRAL has a sparser point cloud, making it more challenging to estimate poses in open areas. In the experiments, the resolution of maps and new scan downsampling size are set to 0.4 m for M2DGR and 0.5 m for NTU VIRAL respectively.

Experiments are carried out on a workstation with Ubuntu 18.04, equipped with an Intel Core Xeon(R) Gold 6248R 3.00GHz processor and 32G RAM.

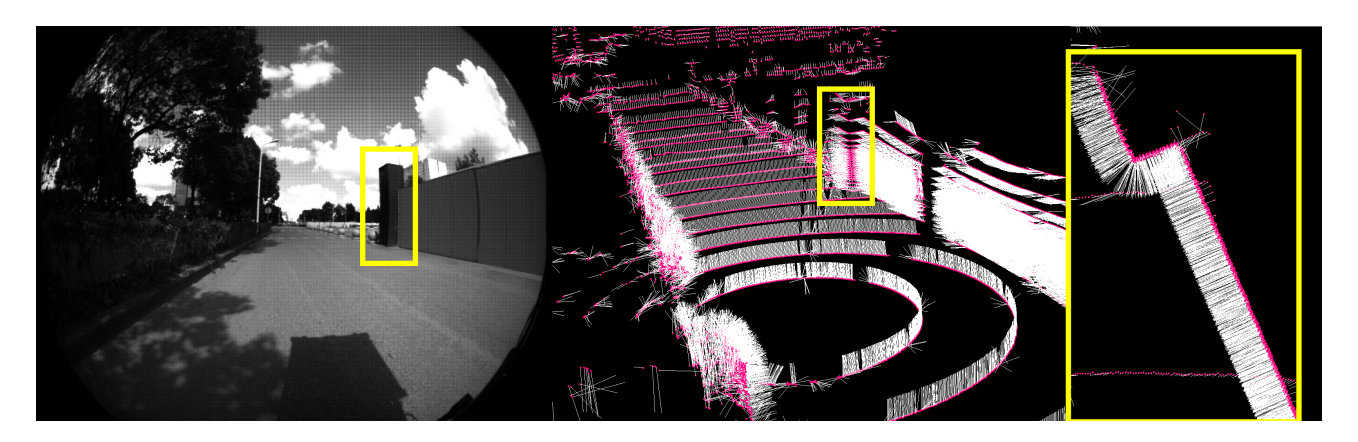


Fig. 3. The starting position of the sequence gate03 of M2DGR dataset. The white lines represent normalized normals from Ring FALS estimation.

 ${\bf TABLE~I}$ The Mean Running Time(MS) of Normal Estimation for A Single Scan to Certain LiDARS

	mainta		Ring FA	PCL			
	points	projection	box-filtering	smoothing	total	single thread	OMP 10 threads
Velodyne-32	57600	2.045	2.540	3.199	7.784	79.811	26.355
Ouster-16	16384	0.560	1.221	0.815	2.597	155.972	39.664

C. Evaluation of Normal Estimation

We conduct a comparative analysis of Ring FALS and PCL [15] normal estimation tools. The implementation of PCL normal estimation is based on traditional least squares with the assistance of kdtree. PCL also provides a parallel implementation using OpenMP [23] to speed up the computation. Note that normal smoothing is a time-consuming process for PCL, so only Ring FALS smoothness the normals.

To provide an intuitive evaluation, we visualize the normals at the starting position of sequence *gate03* of the M2DGR dataset. As shown in Figure 3, the white lines represent the normalized normals estimated by Ring FALS. Notably, almost all ground point normals exhibit a vertical upward orientation. With respect to the pillar in the yellow box, the normals at the corners transit smoothly with the normals on the adjacent sides.

Table I shows the average processing times of normal estimation for a single LiDAR scan from the M2DGR and NTU VIRAL datasets, respectively. The M2DGR dataset contains about 57,600 points per scan. Ring FALS demonstrates significantly reduced processing time compared to PCL, accounting for one-tenth of the time consumed by PCL, and one-fourth compared to the OpenMP version. For NTU VIRAL, Ring FALS also exhibits substantially lower processing time compared to PCL, regardless of whether the OpenMP is used or not.

It is noteworthy that despite the Ouster-16 LiDAR having fewer points than Velodyne-32 in one scan, the consumption time increases. The reason is attributed to the fact that one of the most time-consuming aspects of PCL normal estimation is the kdtree neighborhood search, whose performance is strongly related to the spatial structure of the kdtree. The spatial structure is affected by the complexity of the envi-

ronment.

D. Evaluation of Odometry

We compare LOG-LIO with two state-of-the-art LiDAR-Inertial SLAM methods, LIO-SAM [4] and FAST-LIO2 [14]. For a fair comparison, we disable the loop closure of LIO-SAM because LOG-LIO and FAST-LIO2 are only odometry methods. The root-mean-square error (RMSE) of the absolute trajectory error (ATE) is adopted to assess the accuracy of poses.

1) M2DGR Datasets: Due to the instability of the RTK signal, the first 100 seconds and the last 100 seconds of street07 and street10 are discarded in the experiment.

We evaluate the proposed method, i.e. LOG, and the proposed method without surfel association, i.e. LOG-C, as ablation experiments.

Table II reports the quantitative results. It can be observed that the accuracy of LOG, LOG-C and FAST-LIO2 is comparable in indoor scenes, i.e. door, hall, and these methods outperform LIO-SAM in most sequences. This attributes to the fact that indoor scenes have an abundance of planar features, which leads to a larger number of map points forming true planes. Consequently, the point-to-plane data association provides effective constraints for pose estimation. Conversely, the point-to-line data association of LIO-SAM becomes less reliable, especially when errors accumulated.

In outdoor sequences, i.e. gate, street, map points are relatively sparse compared to indoor scenes. This is especially evident in the *street* sequences, where the robot moves on wide campus roads at night. Figure 4 shows the trajectories of sequence *street10* for qualitative comparison. The superior performance of LOG demonstrates that association with surfels offers a more accurate utilization of local geometric information in scenes with sparse points. On the other

hand, the instability of point-to-line and point-to-plane data associations may lead to the poor performance of LIO-SAM. Overall, only with the visibility and consistency checks, LOG-C slightly improves the average accuracy compared to FAST-LIO2. When considering our proposed hierarchical data association and map management scheme, LOG achieves the lowest error in 13 of the 21 sequences.

Seq	duration (s)	LOG	LOG-C	LIO-SAM	FAST-LIO2	
gate01	172	0.137	0.133	0.170	0.134	
gate02	327	0.290	0.304	0.318	0.304	
gate03	283	0.108	0.108	0.110	0.110	
walk01	291	0.079	0.082	0.078	0.091	
door01	461	0.250	0.250	0.271	0.253	
door02	127	0.178	0.178	0.185	0.178	
street01	1028	0.212	0.212	0.586	0.221	
street02	1227	2.537	2.315	3.619	2.394	
street03	354	0.140	0.146	0.149	0.140	
street04	858	0.525	0.591	1.022	0.568	
street05	469	0.342	0.310	0.491	0.319	
street06	494	0.392	0.437	0.373	0.439	
street07	829	2.301	3.468	1.514	3.422	
street08	491	0.169	0.179	0.212	0.182	
street09	907	3.010	3.570	2.447	3.613	
street10	810	0.329	1.213	8.097	1.256	
hall01	351	0.256	0.257	0.287	0.257	
hall02	128	0.275	0.275	0.290	0.279	
hall03	164	0.340	0.343	0.612	0.346	
hall04	181	0.943	0.943	1.078	0.945	
hall05	402	1.047	1.046	1.010	1.046	
mean		0.660	0.779	1.091	0.786	

2) NTU VIRAL Datasets: As depicted in Table III, LOG-LIO demonstrates the best performance in most sequences, closely followed by FAST-LIO2. On the contrary, LIO-SAM fails more often due to the sparsity of point cloud map. In the sequences nya and tnp, where the drone traverses in confined indoor spaces, both LOG-LIO and FAST-LIO2 exhibit similar errors, showing the behavior observed in M2DGR. Conversely, for the sequences eee, sbs and rtp, despite being outdoor scenes, the drone operated amidst buildings. Consequently, the trajectories obtained from both LOG-LIO and FAST-LIO2 are highly similar due to the effective constraints imposed by the plane structure. However, in the spms sequences, the drone departs from an area surrounded by buildings and subsequently ascends to an altitude higher than the surrounding buildings. Consequently, the sparse point cloud obtained by the horizontally installed LiDAR results in limited overlap with the map, leading to a potentially significant registration error when employing point-to-plane data association. In the case of LOG-LIO, the points are initially associated with the corresponding voxels in which they reside, and the results show that the proposed hierarchical association leads to more reliable constraints, thus enhancing the overall quality of the result.

3) Processing Time Evaluation: We conduct statistical analysis on the average time consumption of LOG-LIO

TABLE III $THE\ TRANSLATION\ RMSE(m)\ RESULTS\ OF\ POSE\ ESTIMATION \\ COMPARISON\ ON\ THE\ NTU\ VIRAL\ DATASET$

Seq	duration	LOG-LIO	FAST-LIO2	LIO-SAM
	(s)			
eee_01	399	0.191	0.193	0.206
eee_02	321	0.141	0.142	0.145
eee_03	181	0.186	0.185	0.206
nya_01	396	0.208	0.204	0.278
nya_02	428	0.212	0.211	0.204
nya_03	411	0.224	0.224	0.305
sbs_01	354	0.222	0.222	x
sbs_02	373	0.208	0.208	0.211
sbs_03	389	0.195	0.194	0.203
rtp_01	482	0.206	0.236	x
rtp_02	453	0.201	0.201	0.182
rtp_03	355	0.195	0.196	0.158
tnp_01	583	0.174	0.171	x
tnp_02	457	0.167	0.167	x
tnp_03	407	0.206	0.202	x
spms_01	446	1.939	1.935	0.600
spms_02	398	2.401	3.388	x
spms_03	386	0.684	0.760	x
mean		0.442	0.502	x

and FAST-LIO2 in each sequence excluding the normal estimation, which is presented in Table IV. It is observed that the average processing time per scan in LOG-LIO is slightly longer than that in FAST-LIO2 due to the incremental maintenance of point distribution within the map voxels. Considering the number of points and the complexity of the environment, LOG-LIO exhibits an additional average time consumption of approximately 5 milliseconds than FAST-LIO2, but it still satisfies the real-time requirements.

VII. CONCLUSION AND FUTURE WORK

This paper proposes LOG-LIO, an online LiDAR-inertial odometry, which incorporates real-time estimation of normal and distribution of points to effectively represent local geometric information. To enhance the efficiency or normal estimation for LiDAR scans, we introduce Ring FALS, an efficient normal estimator that pre-records the structural information and uses only the range information to estimate the point normal. In LOG-LIO, the map is managed using an extended ikd-tree, and the normal and distribution of points within the map voxels are incrementally maintained. By employing a hierarchical data association scheme, accurate constraints are obtained, resulting in more precise pose estimation. Experimental results demonstrate that LOG-LIO outperforms state-of-the-art LIO systems in various environments

For future research, we intend to incorporate dynamic noise removal and loop closure into LOG-LIO to enhance stability in dynamic environments and ensure its long-term operation.

REFERENCES

[1] T. Qin, P. Li, and S. Shen, "Vins-mono: A robust and versatile monocular visual-inertial state estimator," *IEEE Transactions on Robotics*, vol. 34, no. 4, pp. 1004–1020, 2018.

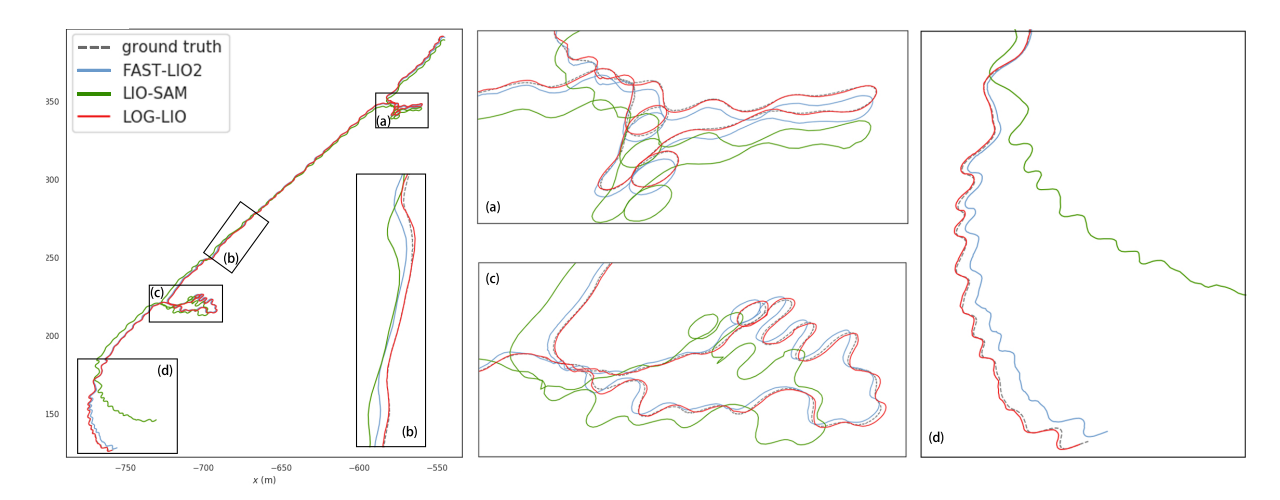


Fig. 4. Localization estimates in sequence *street10* of the M2DGR dataset. The zoomed in image of the colored boxes corresponds to the boxes of the same color in the trajectory.

TABLE IV $\label{thm:local_thm}$ The Average Time Consumption(ms) of Each Sequence in The Experiments

	M2DGR				NTU VIRAL							
	gate	walk	door	street	hall	eee	nya	sbs	rtp	tnp	spms	mean
LOG-LIO	39.839	40.382	18.073	36.380	18.603	18.806	15.421	15.724	23.530	17.122	20.948	25.321
FAST-LIO2	31.378	32.276	14.754	28.970	15.509	15.705	12.476	12.785	21.006	13.340	17.106	20.523

- [2] P. Geneva, K. Eckenhoff, W. Lee, Y. Yang, and G. Huang, "Openvins: A research platform for visual-inertial estimation," in 2020 IEEE International Conference on Robotics and Automation (ICRA). IEEE, 2020, pp. 4666–4672.
- [3] C. Campos, R. Elvira, J. J. G. Rodríguez, J. M. Montiel, and J. D. Tardós, "Orb-slam3: An accurate open-source library for visual, visual-inertial, and multimap slam," *IEEE Transactions on Robotics*, vol. 37, no. 6, pp. 1874–1890, 2021.
- [4] T. Shan, B. Englot, D. Meyers, W. Wang, C. Ratti, and D. Rus, "Lio-sam: Tightly-coupled lidar inertial odometry via smoothing and mapping," in 2020 IEEE/RSJ international conference on intelligent robots and systems (IROS). IEEE, 2020, pp. 5135–5142.
- [5] K. Chen, B. T. Lopez, A.-a. Agha-mohammadi, and A. Mehta, "Direct lidar odometry: Fast localization with dense point clouds," *IEEE Robotics and Automation Letters*, vol. 7, no. 2, pp. 2000–2007, 2022.
- [6] T.-M. Nguyen, D. Duberg, P. Jensfelt, S. Yuan, and L. Xie, "Slict: Multi-input multi-scale surfel-based lidar-inertial continuoustime odometry and mapping," *IEEE Robotics and Automation Letters*, vol. 8, no. 4, pp. 2102–2109, 2023.
- [7] J. Zhang and S. Singh, "Loam: Lidar odometry and mapping in realtime." in *Robotics: Science and Systems*, vol. 2, no. 9. Berkeley, CA, 2014, pp. 1–9.
- [8] A. Reinke, M. Palieri, B. Morrell, Y. Chang, K. Ebadi, L. Carlone, and A.-A. Agha-Mohammadi, "Locus 2.0: Robust and computationally efficient lidar odometry for real-time 3d mapping," *IEEE Robotics and Automation Letters*, vol. 7, no. 4, pp. 9043–9050, 2022.
- [9] M. Palieri, B. Morrell, A. Thakur, K. Ebadi, J. Nash, A. Chatterjee, C. Kanellakis, L. Carlone, C. Guaragnella, and A.-a. Agha-Mohammadi, "Locus: A multi-sensor lidar-centric solution for high-precision odometry and 3d mapping in real-time," *IEEE Robotics and Automation Letters*, vol. 6, no. 2, pp. 421–428, 2020.
- [10] M. Ramezani, K. Khosoussi, G. Catt, P. Moghadam, J. Williams, P. Borges, F. Pauling, and N. Kottege, "Wildcat: Online continuoustime 3d lidar-inertial slam," arXiv preprint arXiv:2205.12595, 2022.
- [11] H. Badino, D. Huber, Y. Park, and T. Kanade, "Fast and accurate computation of surface normals from range images," in 2011 IEEE International Conference on Robotics and Automation. IEEE, 2011, pp. 3084–3091.
- [12] R. Fan, H. Wang, B. Xue, H. Huang, Y. Wang, M. Liu, and I. Pitas, "Three-filters-to-normal: An accurate and ultrafast surface normal

- estimator," *IEEE Robotics and Automation Letters*, vol. 6, no. 3, pp. 5405–5412, 2021.
- [13] W. Xu and F. Zhang, "Fast-lio: A fast, robust lidar-inertial odometry package by tightly-coupled iterated kalman filter," *IEEE Robotics and Automation Letters*, vol. 6, no. 2, pp. 3317–3324, 2021.
- [14] W. Xu, Y. Cai, D. He, J. Lin, and F. Zhang, "Fast-lio2: Fast direct lidar-inertial odometry," *IEEE Transactions on Robotics*, vol. 38, no. 4, pp. 2053–2073, 2022.
- [15] R. B. Rusu and S. Cousins, "3d is here: Point cloud library (pcl)," in 2011 IEEE international conference on robotics and automation. IEEE, 2011, pp. 1–4.
- [16] A. Segal, D. Haehnel, and S. Thrun, "Generalized-icp." in *Robotics: science and systems*, vol. 2, no. 4. Seattle, WA, 2009, p. 435.
- [17] M. Kaess, H. Johannsson, R. Roberts, V. Ila, J. J. Leonard, and F. Dellaert, "isam2: Incremental smoothing and mapping using the bayes tree," *The International Journal of Robotics Research*, vol. 31, no. 2, pp. 216–235, 2012.
- [18] C. Yuan, X. Liu, X. Hong, and F. Zhang, "Pixel-level extrinsic self calibration of high resolution lidar and camera in targetless environments," *IEEE Robotics and Automation Letters*, vol. 6, no. 4, pp. 7517–7524, 2021.
- [19] C. Yuan, W. Xu, X. Liu, X. Hong, and F. Zhang, "Efficient and probabilistic adaptive voxel mapping for accurate online lidar odometry," *IEEE Robotics and Automation Letters*, vol. 7, no. 3, pp. 8518–8525, 2022
- [20] L. Zhou, D. Koppel, and M. Kaess, "Lidar slam with plane adjustment for indoor environment," *IEEE Robotics and Automation Letters*, vol. 6, no. 4, pp. 7073–7080, 2021.
- [21] J. Yin, A. Li, T. Li, W. Yu, and D. Zou, "M2dgr: A multi-sensor and multi-scenario slam dataset for ground robots," *IEEE Robotics and Automation Letters*, vol. 7, no. 2, pp. 2266–2273, 2021.
- [22] T.-M. Nguyen, S. Yuan, M. Cao, Y. Lyu, T. H. Nguyen, and L. Xie, "Ntu viral: A visual-inertial-ranging-lidar dataset, from an aerial vehicle viewpoint," *The International Journal of Robotics Research*, vol. 41, no. 3, pp. 270–280, 2022.
- [23] R. Chandra, L. Dagum, D. Kohr, R. Menon, D. Maydan, and J. Mc-Donald, *Parallel programming in OpenMP*. Morgan kaufmann, 2001.